Dalton Transactions

ROYAL SOCIETY OF CHEMISTRY

PAPER

View Article Online
View Journal | View Issue

Cite this: *Dalton Trans.*, 2020, **49**, 10477

An investigation into the magnetic interactions in a series of Dy_2 single-molecule magnets†

Chaoyi Jin,[a,b] Xiao-Lei Li,[a] Zhiliang Liu,[b] Akseli Mansikkamäki *[c] and Jinkui Tang *[a,d]

Received 29th May 2020,
Accepted 7th July 2020

DOI: 10.1039/d0dt01926g

rsc.li/dalton

Three di-nuclear Dy^{III} complexes $[Dy_2(H_2L)_2(tfa)]\cdot Cl\cdot 3DMF$ (**1**), $[Dy_2(H_2L)_2(MeO)(SCN)]\cdot MeOH$ (**2**) and $[Dy_2(H_2L)_2(MeOH)Cl]\cdot Cl\cdot 2MeOH$ (**3**) were synthesized and structurally and magnetically characterized. The Dy1/Dy2 centers in these complexes are all nine-coordinate with spherical capped square antiprism (local C_4v symmetry) environments. All complexes display single-molecule magnet (SMM) behavior under zero applied dc field with their properties dependent on the nature of the magnetic interactions between the Dy^{III} ions. *Ab initio* calculations substantiate that all Dy^{III} ions show a weakly axial crystal-field environment with the exception of one of the Dy^{III} ions in complex **2**. The ground Kramers doublets show modest amounts of quantum tunneling of magnetization that gets blocked by the interaction between the Dy^{III} ions, leading to a thermally activated slow relaxation of magnetization. The interaction between the ions is ferromagnetic and mostly originates from the dipolar interaction. However, anti-ferromagnetic intermolecular interaction plays an important role and in the case of complex **2** it is sufficiently strong to mask the ferromagnetic intramolecular interaction.

Introduction

Single-molecule magnets (SMMs) are molecules with nanomagnetic functionality.[1–5] Unlike classical ferromagnetism, the magnetic behavior is characterized by slow relaxation of magnetization of individual molecules rather than the collective behavior of an ensemble of paramagnetic atoms in a magnetic domain. As a result, SMMs have been suggested as ideal candidates for potential applications in related areas of technological development such as high-density information storage, molecular spintronic devices and quantum computations.[6] One of the key challenges to the application of SMMs in quantum technologies is their operational temperature, which is usually very low. Recently, chemists have been pursuing high energy barriers (U_{eff}) and blocking temperatures (T_B) for potential applications in molecular devices.[7,8] Because of the strong magnetic anisotropy induced by its strong spin–orbit coupling, lanthanide ions are considered to be good candidates for constructing SMMs since the initial discovery of slow relaxation of magnetization in a series of $[NH_4][LnPc_2]$ lanthanide complexes in 2003.[9–11] Among all mononuclear lanthanide SMMs currently studied, the complex $[(Cp^{iPr5})Dy(Cp^*)][B(C_6F_5)_4]$ has the highest blocking temperature of 80 K.[12] However, the efficient quantum tunneling of magnetization (QTM) in mononuclear lanthanide SMMs usually causes a rapid decay of magnetization at zero field, resulting in a decrease or even disappearance of remanence and coercivity in the respective hysteresis loops. Intramolecular magnetic coupling interactions in polymetallic lanthanide systems can often efficiently suppress the QTM, leading to considerably long relaxation times also at zero field.[13–19]

Under appropriate conditions, coordination complexes can be assembled into regularly ordered structures through various non-covalent interactions such as metal coordination, hydrogen bonding and van der Waals interactions. Herein, we prepared three isomorphous di-nuclear Dy^{III} complexes with different coordination anions and molecular packing modes using the Schiff base ligand (*E*)-6-((bis(2-hydroxyethyl)amino)methyl)-*N*′-(2-hydroxy-3-methoxybenzylidene)picolinohydrazide (H_4L, Fig. 1, top left) in order to probe how the changes in the crystal field experienced by the Dy^{III} ions affect their SMM properties.[20–22] All of the complexes show a thermally activated slow relaxation of magnetization. Intriguingly, anti-ferro-

[a]*State Key Laboratory of Rare Earth Resource Utilization, Changchun Institute of Applied Chemistry, Chinese Academy of Sciences, Changchun, 130022, P. R. China. E-mail: tang@ciac.ac.cn*
[b]*College of Chemistry and Chemical Engineering, Inner Mongolia University, Hohhot, 010021, China*
[c]*NMR Research Unit, University of Oulu, P.O. Box 8000, Finland. E-mail: Akseli.Mansikkamaki@oulu.fi*
[d]*School of Applied Chemistry and Engineering, University of Science and Technology of China, Hefei, 230026, P. R. China*

†Electronic supplementary information (ESI) available: Experimental details, structural figures, crystallographic data, magnetic and spectroscopic characterization. CCDC 1999025 (**1**), 1999026 (**2**), 1999103 (**3**). For ESI and crystallographic data in CIF or other electronic format see DOI: 10.1039/D0DT01926G

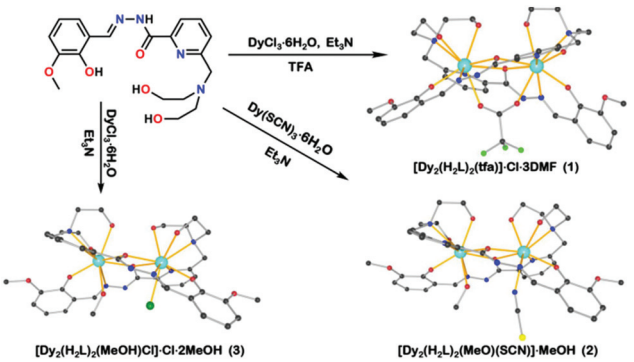

Fig. 1 Synthesis and perspective view of the structures of compounds **1–3**. Color code: turquoise, Dy; blue, N; red, O; bright green, F; green, Cl; yellow, S; gray, C. Hydrogen atoms and solvent molecules have been omitted for the sake of clarity.

magnetic intermolecular interaction in the case of one of the complexes is sufficiently strong to mask the ferromagnetic intramolecular interaction, leading to overall antiferromagnetic interactions.

Experimental section

General information

All chemicals used throughout the experiments were commercially available with analytical grade and used as received without any further purification, where all manipulations were also performed under an aerobic environment.

Synthesis of ligand

The Schiff base ligand H_4L was prepared by a refluxing of 2-hydroxy-3-methoxybenzaldehyde and 6-((bis(2-hydroxyethyl) amino)methyl)picolinohydrazide in a 1 : 1 ratio in methanol according to a literature procedure.[23]

Synthesis of $[Dy_2(H_2L)_2(tfa)]\cdot Cl\cdot 3DMF$ (1). $DyCl_3\cdot 6H_2O$ (0.1 mmol) was added to a solution of H_4L (0.15 mmol) in a 15 mL mixture of methanol and acetonitrile (1/2, v/v), and triethylamine (40 μL) was added after stirring for 15 minutes. Then, trifluoroacetic acid (tfa, 0.15 mmol) was added to the mixture and the resultant solution was stirred for 4 h and filtered subsequently, affording a yellow solution. The filtrate was exposed to air to allow the slow evaporation of the solvent. The solid was collected after the solvent was evaporated out and dissolved in 10 ml DMF, followed by the slow diffusion of diethyl ether. Bright yellow crystals suitable for X-ray diffraction were obtained over one week. Yield 0.023 g, (61%, based on Dy). Elemental analysis (%) calcd for $C_{49}H_{65}Dy_2N_{11}O_{15}$ (M_W = 1465.57): C, 40.16; H, 4.47; N, 10.51. Found: C, 40.12; H, 4.43; N, 10.41.

Synthesis of $[Dy_2(H_2L)_2(MeO)(SCN)]\cdot MeOH$ (2). $Dy(SCN)_3\cdot 6H_2O$ (0.15 mmol) was added to a solution of H_4L (0.1 mmol) in a 15 mL mixture of methanol and acetonitrile (1/2, v/v), and then triethylamine (40 μL) was added after stirring for 15 minutes. The resultant solution was allowed to stir for 4 h and then filtered out, affording a yellow solution. The filtrate was exposed to air to allow the slow evaporation of the solvent. Bright yellow crystals suitable for X-ray diffraction were obtained over two weeks. Yield 0.02 g, (46%, based on Dy). Elemental analysis (%) calcd for $C_{41}H_{51}Dy_2N_9O_{12}S$ (M_W = 1218.97): C, 40.41; H, 4.20; N, 10.34. Found: C, 40.38; H, 4.18; N, 10.31.

Synthesis of $[Dy_2(H_2L)_2(MeOH)Cl]\cdot Cl\cdot 2MeOH$ (3). $DyCl_3\cdot 6H_2O$ (0.1 mmol) was added to a solution of H_4L (0.1 mmol) in a 15 mL mixture of methanol and acetonitrile (1/2, v/v), and then triethylamine (40 μL) was added after stirring for 15 minutes. The resultant solution was allowed to stir for 4 h and then filtered out, affording a yellow solution. The solvent was removed under vacuum to give a yellow solid, which was washed with diethyl ether and re-dissolved in methanol. Diethyl ether was allowed to slowly diffuse into the system. Bright yellow crystals suitable for X-ray diffraction were obtained over one week. Yield 0.016 g, (42%, based on Dy). Elemental analysis (%) calcd for $C_{41}H_{56}Cl_2Dy_2N_8O_{13}$ (M_W = 1264.83): C, 38.93; H, 4.46; N, 8.86. Found: C, 38.91; H, 4.43; N, 8.85.

Crystallography

The structures of **1–3** were determined at 173 K on a Bruker AXS D8 Venture single-crystal diffractometer equipped with graphite-monochromatized Cu Kα radiation (λ = 1.542 Å). The structures were determined with the ShelXT[24] structure solution program using the Intrinsic Phasing solution method and by using Olex2 [25,26] as the graphical interface. The model was refined with a version of ShelXL[24] using Least Squares minimisation. All non-hydrogen atoms were refined anisotropically. Most hydrogen atom positions were calculated geometrically and refined using the riding model, but some hydrogen atoms were refined freely.

Magnetic susceptibility measurements

Magnetic data were obtained by using a Quantum Design MPMS XL-7 SQUID magnetometer equipped with a 7 T magnet at the temperature range of 2–300 K. The experimental magnetic data were corrected for the diamagnetism of the constituent atoms using Pascal's tables[27] and by sample holder calibration.

Computational details

The geometries were extracted from the crystal structure and the positions of the hydrogen atoms were optimized using density functional theory (DFT) while the positions of the heavier atoms were kept frozen to their crystal-structure coordinates. The DFT optimizations were carried out using the Gaussian 09 quantum chemistry software revision E.01 and the hybrid PBE0 exchange–correlation (XC) functional.[28–31] A 4f-in-core MWB55 effective core potential (ECP) along with a corresponding valence basis set[32,33] was used for the Dy ions and Ahlrichs' valence-polarized triple-ζ basis[34] was used for the other atoms. The quality of the integration grid was set to

"UltraFine" in Gaussian and the accuracy of the two-electron integrals was raised to 10^{-12} atomic units.

Ab initio calculations were carried out on each Dy^{III} center in the three complexes. First, a set of state-averaged (SA) complete active space self-consistent field (CASSCF) calculations[35–37] were carried out. All 21 sextet, 224 quartet and 490 doublet states were solved in three separate calculations. The effects of spin–orbit coupling (SOC) were then introduced using the restricted active space state-interaction (SO-RASSI) approach.[38] The SOC operator was constructed in a basis consisting of 21 sextet, 128 quartet and 130 doublet states corresponding to an energy cut-off of 50 000 cm^{-1}. The single-ion magnetic properties were calculated using the SINGLE-ANISO routine[39,40] and the intersite properties were calculated using the POLY-ANISO routine.[41–44]

The *ab initio* calculations were carried out using Molcas quantum chemistry software version 8.4.[45] Scalar relativistic effects were introduced using the exact two-component (X2C) transformation[46,47] as implemented in Molcas. Relativistically contracted atomic natural orbital (ANO-RCC) basis sets were used throughout.[48–50] A valence-polarized triple-ζ quality (VTZP) basis was used for the Dy ions and a valence-polarized double-ζ quality (VDZP) was used for the other atoms. The two-electron integrals were stored using the Cholesky decomposition with a threshold of 10^{-8} atomic units.

Broken symmetry (BS)[51–54] DFT exchange coupling constants were calculated using the Gaussian code and the range-separated hybrid XC functional CAM-B3LYP.[55–57] The Dy^{III} ions were replaced by Gd^{III} ions. Dolg's small-core ECP[32] was used to treat the core electrons of the Gd^{III} ion. The valence orbitals in the Gd^{III} and other atoms were treated using the valence-triple-ζ quality def2-TZVP basis.[58,59] The exchange coupling constant for the Gd^{III} system was extracted by calculating the M_S = 0 and M_S = 7 solutions and mapping these to diagonal elements of the Heisenberg–Dirac–van Vleck Hamiltonian. The exchange coupling constants are then given by

$$J_{\text{exchange,Gd-Gd}} = {}^{8}/_{49}(E_{\text{LS}} - E_{\text{HS}})$$

where E_{LS} and E_{HS} are the BS energies of the M_S = 0 and M_S = 7 solutions, respectively. A stability analysis was carried out on all solutions to ensure that they correspond to true minima in the molecular orbital coefficient space.[60,61] The calculated exchange coupling constants were related to those of the analogous Dy^{III} system by scaling them from the S = 7/2 spin of the Gd^{III} ions to the S = 5/2 spin of the Dy^{III} ions:[62]

$$J_{\text{exchange,Dy-Dy}} = \frac{(7/2)^2}{(5/2)^2} J_{\text{exchange,Gd-Gd}} = \frac{49}{25} J_{\text{exchange,Gd-Gd}}$$

Results and discussion

Crystallography

Complexes **1–3** were characterized by single-crystal X-ray diffraction, revealing that **1–3** are all di-nuclear complexes crystallized in the monoclinic space group $P2_1/c$. Details of the crystallographic data and structural solutions are summarized in Table S1,† and the selected bond lengths and angles are listed in Table S2.†

The structures of the three complexes are similar, consisting of two Dy^{III} ions and two dianionic H_2L^{2-} ligands in each structure. Each of the two Dy^{III} ions was bound by two H_2L^{2-} ligands, through the systematically designed asymmetric pockets with the connection of a bridging enolate oxygen. The remaining coordination sites are completed by one tfa^- anion for **1**, one SCN^- anion and a methoxy anion for **2**, and one Cl^- anion and a MeOH molecule for **3**, respectively (Fig. 1). The assignment of the methoxy anion in **2** is based on charge balance and the longer Dy–O distance (2.458 Å) in **2** than that detected in **3** (2.433 Å). Thus complex **2** is neutral, while **1** and **3** are positively charged with an extra counter anion (Cl^-) co-crystalized in each compound. Accurate geometry analysis by SHAPE 2.0 software[63] (Table S3†) reveals that each of the Dy^{III} ions in complexes **1–3** is nine-coordinate with a spherical capped square antiprism (local C_{4v}) geometry (Fig. 2). The Dy–O bond lengths are in the ranges of 2.183(4)–2.527(4), 2.223(3)–2.540(3) and 2.199(4)–2.558(4) Å for complexes **1–3**, respectively. The Dy–N bond lengths are in the ranges of 2.502(5)–2.697(5), 2.491(4)–2.633(4) and 2.474(5)–2.685(5) Å for complexes **1–3**, respectively.

Complexes **1–3** display almost the same dimer structure stacked through the hydrogen bond in a trans fashion. In the dimers, the protonated diethanolamine moieties in the molecules act as O-donors, while N atoms of the deprotonated hydrazine moieties act as acceptors. The shortest intermolecular Dy···Dy distance is in the range of 7.252–7.503 Å. It should be noted that the shortest intermolecular Dy···Dy distances do not preclude possible intermolecular magnetic interactions in any of the complexes. Interestingly, the dimers of all the complexes were further connected by intermolecular hydrogen bonding to accomplish different types of crystallographic arrangements (Fig. 3 and S1†).

For complex **1**, the dimers are accumulated linearly along the crystallographic *a*-axis, creating a one-dimensional chain (Fig. 3 top and S2†) through the same kind of "N···H–O" hydrogen bond interactions as observed within the dimer. For

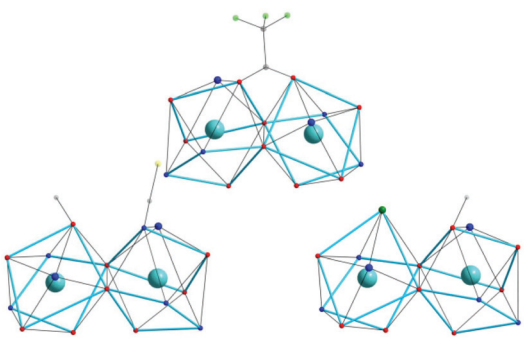

Fig. 2 The coordination environments of Dy^{III} ions for **1** (top), **2** (bottom left) and **3** (bottom right).

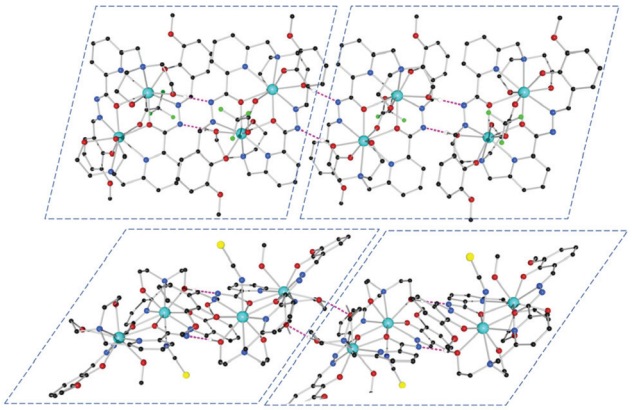

Fig. 3 Multiple intermolecular hydrogen bondings (pink dotted lines) in **1** (top), **2** (bottom).

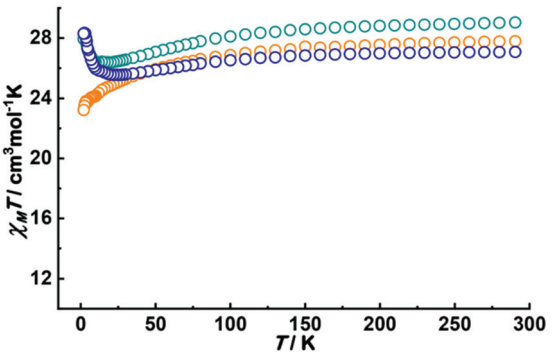

Fig. 4 Temperature dependence of the $\chi_M T$ products at 1 kOe for **1** (green), **2** (orange) and **3** (blue).

complex **2**, the one-dimensional chains are formed *via* a new type of intermolecular hydrogen-bonds (Fig. 3 bottom). The entire chain structure extends along the direction of the diagonal of *a*-axis and *c*-axis (Fig. S2†). The donor and acceptor atoms of the hydrogen bonds that form the dimer pairs are all the oxygen atoms located in the equivalent position of the diethanolamine moiety from adjoining ligands. As for complex **3**, the dimer pairs are separated further from each other by three kinds of hydrogen bonds. In this way the dimer pairs are no longer ordered in one direction, but in a two-dimensional sheet[64] (Fig. S1†), and packed layer by layer in the lattice (Fig. S3†). The hydrogen bonds linking the "dimers" together originate from Cl^- anions, MeOH molecules and hydroxyl oxygen atoms. Cl^- is bound to two O-donors that originated from a diethanolamine of one dimer and a guest MeOH molecule around it. Meanwhile, MeOH is also employed as an acceptor of the other O-donor that belongs to the next dimer. For all complexes, the shortest Dy···Dy distances between the dimer pairs are 7.482, 6.258 and 9.940 Å for **1**, **2** and **3**, respectively, which range wider than that within the dimers. It is worth noting that the new type of hydrogen bond in **2** is unique considering that the O-donors and O-accepters participate in coordination at the same time. In this way, the adjacent Dy centers of two units are held much closer (6.258 Å) directly by the "O···H–O" hydrogen bond, affording a "Dy–O···H–O–Dy" connection, which may have a critical effect on the intermolecular magnetic interactions of compounds (see the calculation part below).

Static magnetic studies

The temperature-dependent molar magnetic susceptibility (χ_M) of complexes **1–3** in the temperature range of 2–300 K is shown in Fig. 4. The values of the $\chi_M T$ product at room temperature for complexes **1–3** are 28.9, 27.7 and 26.9 cm^3 K mol^{-1}, respectively, which are close to the theoretical value of 28.34 cm^3 K mol^{-1} for two noninteracting Dy^{III} ions ($^6H_{15/2}$, S = 5/2, L = 5, J = 15/2, g = 4/3). As the temperature decreases, the $\chi_M T$ values of **1–3** gradually decrease due to thermal depopulation of excited states in the crystal-field split ground $^6H_{15/2}$ multiplet of the Dy^{III} ions. Below 10 K, the $\chi_M T$ products of **1** and **3** increase sharply, reaching 27.9 and 28.2 cm^3 K mol^{-1} at 2 K, respectively, suggesting the existence of ferromagnetic interactions. On the other hand, for complex **2**, the drop in $\chi_M T$ below 3 K suggests the presence of overall antiferromagnetic interactions (see the calculation part below).[65]

The molar magnetization (M) of **1–3** was measured at different temperatures and in the magnetic field (H) varying between 0 and 70 kOe. As shown in Fig. S4,† at low fields, the magnetization rapidly increases, suggesting the existence of ferromagnetic interactions, and then settles to a slow linear increase at 10 kOe. The magnetization does not saturate at the theoretical value of two Dy^{III} ions 20μ_B (for the Dy^{III} ion, $g_J \times J$ = (4/3) × (15/2) = 10μ_B) within the measurement range. Furthermore, the isothermal magnetization measured as a function of field measured at different temperatures for **1–3** does not superimpose completely, suggesting the possibility of a low-lying excited state arising from the exchange interaction.[66] No obvious magnetic hysteresis was observed above 1.9 K (Fig. S5†).

Dynamic susceptibility studies

Dynamic alternating current (ac) magnetic susceptibility measurements were carried out for complexes **1–3** under a 3 Oe oscillating field and zero DC field. Strong frequency- and temperature-dependent in-phase (χ') and out-of-phase (χ'') signals with peaks were observed in the corresponding frequency and temperature range for all three complexes, indicating slow magnetic relaxation typical to SMMs for all complexes (Fig. 5 and S6†). It is worth mentioning that QTM behavior was not clearly observed even at a temperature as low as 1.9 K.

Furthermore, a clearer difference of the relaxation process among these three complexes was observed in the χ'' *versus* T plots (Fig. S6†). For complex **3**, the out-of-phase peaks at high temperatures reveal the presence of a single relaxation process. While for complex **1**, a weak shoulder of a peak in χ'' at 15 K appears besides the first peak at 11 K between 320 Hz and 1488 Hz (Fig. S6†), implying the possible occurrence of two relaxation processes. For complex **2**, the plots show a more pro-

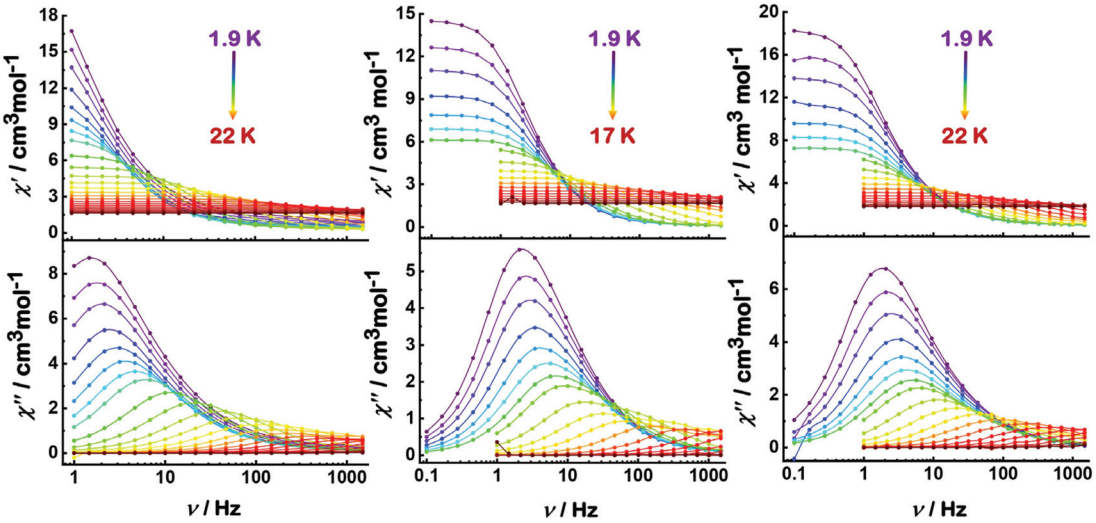

Fig. 5 Frequency dependence of the in-phase and out-of-phase ac susceptibilities under zero dc field for complexes **1** (left), **2** (middle) and **3** (right).

nounced double peak feature in the high frequency region, implying the possible occurrence of two relaxation processes, which is not uncommon in polynuclear dysprosium compounds.[14,67] To evaluate the relaxation barrier (U_{eff}/k_B), the relaxation time (τ) was extracted from χ'' (ν) data by using the generalized Debye model for **1** and **3** and by using the sum of two modified Debye functions for **2**:[68]

$$\chi_{ac}(\omega) = \chi_{S1} + \chi_{S2} + \frac{\chi_{T1} - \chi_{S1}}{1 + (i\omega\tau_1)^{(1-\alpha_1)}} + \frac{\chi_{T2} - \chi_{S2}}{1 + (i\omega\tau_2)^{(1-\alpha_2)}}$$

It is worth noting that the relaxation times of **1** and **3** exhibit temperature-dependent behavior over the whole temperature range (Fig. 6), suggesting that the relaxation process is dominated by the Orbach mechanism at high temperatures and the Raman mechanism at low temperatures rather than the direct and quantum tunneling effects, even at 1.9 K. The Arrhenius plots of ln τ *vs.* $1/T$ should show linear behavior at high temperature due to a thermally activated Orbach process. As the first step in the fitting, the Arrhenius plot was fitted with the equation

$$\tau = \tau_0 \exp(U_{eff}/k_B T) \quad (1)$$

at high temperature. The effective energy barrier (U_{eff}) and the pre-exponential factor (τ_0) are 90.57 K ($\tau_0 = 3.01 \times 10^{-7}$ s) and 81.39 K ($\tau_0 = 9.18 \times 10^{-8}$ s) for **1** and **3**, respectively. In order to provide a complete picture of the relaxation mechanisms over the whole temperature range, as a second step, the data were fitted by the equation:

$$\ln \tau = -\ln[CT^n + \tau_0^{-1} \exp(-U_{eff}/k_B T)], \quad (2)$$

where CT^n and $\tau_0^{-1}\exp(U_{eff}/k_B T)$ represent Raman and Orbach relaxation processes, respectively. The new fitting gave the

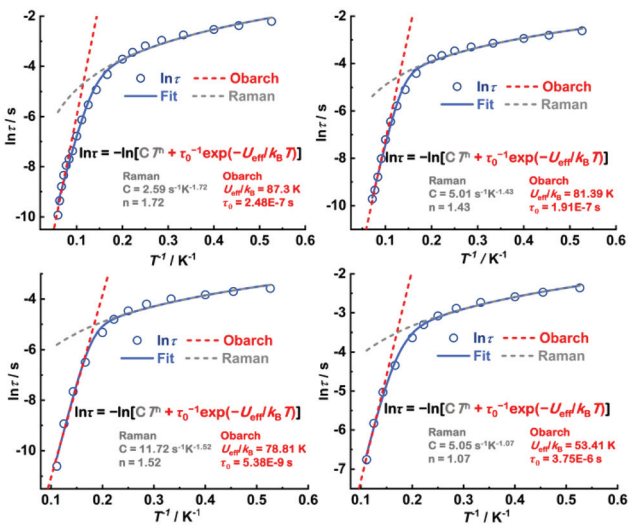

Fig. 6 Plots of ln τ *versus* T^{-1} for **1** (top left), **3** (top right), **2** FR (bottom left) and **2** SR (bottom right) under zero dc field.

effective energy barriers of 87.25 K ($\tau_0 = 2.48 \times 10^{-7}$ s) and 81.39 K ($\tau_0 = 1.91 \times 10^{-7}$ s) for **1** and **3**, respectively. The other parameters are collected in Table S4. For complex **2**, the same equation was used to fit the plot. The fit yielded the energy barriers of 78.81 and 53.41 K with pre-exponential factors of 5.38×10^{-9} and 3.75×10^{-6} s for the fast relaxation (FR) and slow relaxation (SR) processes of **2**, respectively.

The Cole–Cole diagrams of **1** (Fig. 7a) and **3** (Fig. 7b) show a semicircular shape that can be fitted by using CC-FIT2 based on the generalized Debye model.[69] This fit provides the parameter α, which is related to the width of the relaxation time distribution. For complexes **1** and **3**, the value of α parameters are found in a range of 0.10–0.23 and 0.16–0.2 (1.9–14 K), respectively, indicating the relatively wide distribution of relax-

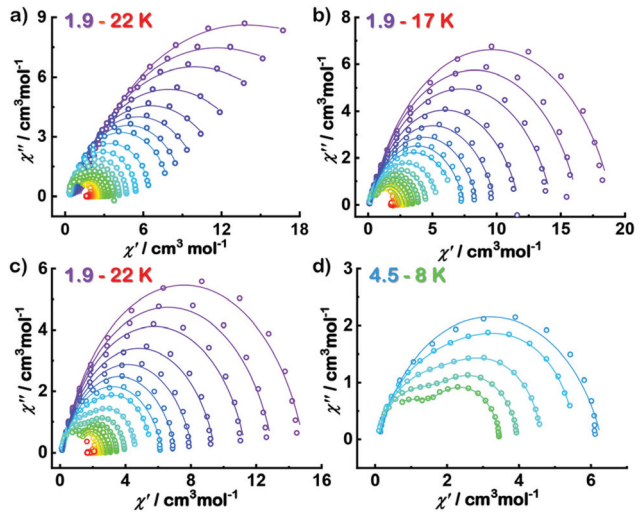

Fig. 7 Cole–Cole diagrams at different temperatures under zero dc field for (a) **1**, (b) **3** and (c) **2**. For the sake of clarity, (d) shows only data for the temperature range from 4.5 to 8 K in **2**. The solid lines in all diagrams represent the best fit obtained.

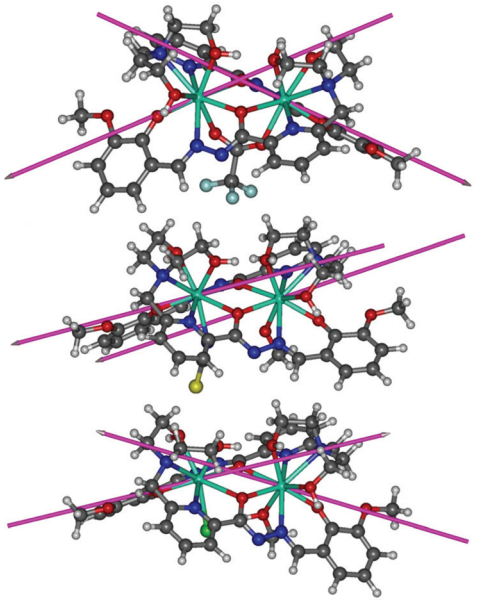

Fig. 8 The principal magnetic axes of the ground Kramers doublets of the two Dy^{III} ions in **1** (top), **2** (middle) and **3** (bottom).

ation times. For complex **2**, two clear relaxation processes are observed in the high temperature region (4.5–8 K) (Fig. 7c, d and S6†). However, as the temperature increases further, the FR was gradually shifted beyond the limit of high-frequency (1488 Hz), leading to only an asymmetric semicircle that belongs to SR after 10 K. By fitting the data to eqn (1), the obtained parameter α is in the range of 0.17–0.19 (1–9 K) and 0.03–0.08 (1–9 K) for FR and SR, respectively. The 3D surface map of the double relaxation process also displays the double ridge phenomenon in the corresponding area (Fig. S7†).

Theoretical calculations

In order to rationalize the abovementioned magnetic behaviors, the magnetic properties of the individual Dy^{III} ions in complexes **1**, **2**, and **3** were calculated using the well-established SA-CASSCF/RASSI-SO methodology.[35–41] The calculated properties of the Dy^{III} ions are rather typical to a weakly axial environment. The only exception is the Dy2 center in complex **2**. In the other cases the ground doublets have axial g-tensors with small but non-negligible transverse components ranging from $g_{x/y}$ = 0.0257 to 0.0662 which are sufficiently large to allow some QTM at zero field. However, the weak intramolecular coupling is sufficient to suppress the QTM and allow slow relaxation of magnetization with a thermally activated mechanism. The ground Kramers doublets are separated from the first excited doublets by 110 cm^{-1} to 148 cm^{-1} and these most likely set the effective barrier heights for the Orbach mechanism. In all cases the values are larger than the effective barrier heights determined from the fits but are still in reasonable agreement. The direction of the principal magnetic axes of the ground doublets (Fig. 8) is determined by the aryloxy oxygen groups in the ligands. The aryloxy groups are strongly basic and determine the strongest crystal-field (CF) direction. More details of the low-lying doublets are given in Tables S5–S7.†

In the case of the Dy2 center in **2**, the situation is somewhat different. The g-tensor has larger transversal components (g_x = 0.3067 and g_y = 1.1655) allowing more significant QTM, which most likely cannot be suppressed by any external field. The first excited doublet also lies at 69 cm^{-1}, which is lower than the other Dy^{III} centers. These differences could have originated from the coordinated methoxy anion. The aryloxy oxygen and the methoxy oxygen groups both induce a strong CF, and the angle between them is only 77.9°, where the CF does not have a single clear strong-field direction, which could lead to a clearly axial CF. Meanwhile, a stronger intermolecular hydrogen bond (formed by the two oxygen atoms participating in the coordination of the Dy2 center) produces a more compact one-dimensional structure of **2**, which has the shortest intermolecular distance of 6.258 Å among the three complexes. Therefore, this significant intermolecular interaction between the Dy2 centers is likely to have facilitated the fast relaxation process in complex **2** which is evident by ac measurements. The calculated results are consistent with those of two Dy^{III} ions that differ in their magnetic properties and lead to two distinct relaxation processes as observed in the ac measurements.

The geometry of the bridging ligands qualitatively supports a ferromagnetic superexchange mechanism between the two Dy^{III} ions. In the case of **1** and **3** a sharp increase in the $\chi_M T$ product is observed at a low temperature, which is in agreement with weak ferromagnetic interaction. In the case of **2**, however, no increase is observed, suggesting an anti-ferromagnetic mechanism. This discrepancy is at odds with the qualitatively similar geometric structure of the bridging

ligands. To get more insight into the interaction mechanism, the intramolecular exchange coupling was first studied by broken symmetry (BS) density functional theory (DFT).[51–54,70] The exchange coupling constants were estimated by calculating the exchange coupling constants of an isostructural Gd^{III} complex and rescaling the calculated values to the spin of the Dy^{III} ions using a previously established approximate approach.[62] The calculated values are $J_{exchange}$ = 0.343 cm^{-1}, $J_{exchange}$ = 1.959 cm^{-1} and $J_{exchange}$ = 0.137 cm^{-1} for **1**, **2** and **3**, respectively, which are in agreement with the weak ferromagnetic superexchange. The value calculated for **2** is significantly larger than that calculated for **1** and **3**. No obvious reason for this discrepancy could be found. Attempts were made to increase the numerical accuracy in the calculations and to try other approximations to the exchange–correlation functional. Since the BS-DFT calculations have been conducted without considering spin–orbit coupling (SOC) and re-scaled from Gd^{III} analogues, the calculated values should be taken more as order-of-magnitude estimates than as quantitative measures. The small values also lie at the very limit of the numerical accuracy of the DFT calculations.

The exchange coupling was then studied using the Lines model and the *ab initio* multireference results. The Lines parameter was fitted by constructing the exchange states from the single-ion *ab initio* results and fitting the resulting magnetic susceptibility to the experimentally measured susceptibility. The overall interaction consists of three components: the superexchange *via* the bridging ligands, dipolar intramolecular coupling between the Dy^{III} ions and intermolecular dipolar coupling due to short intermolecular contacts, that is $J_{total} = J_{exchange} + J_{dipolar} + J_{inter}$. The intramolecular dipolar coupling can be described by an Ising-type Hamiltonian operating on the ground KDs of the two ions described by $\tilde{S}$ = 1/2 pseudospin:

$$\hat{H}_{dipolar} = -J_{dipolar}\tilde{S}_{1z}\tilde{S}_{2z}$$

where $J_{dipolar}$ is the dipolar coupling parameter and $\tilde{S}_{1z}$ and $\tilde{S}_{2z}$ are pseudospin operators acting on the projection of the pseudospin of the ground KD onto the local quantization axis at ions Dy1 and Dy2, respectively. The coupling parameters are $J_{dipolar}$ = 4.512 cm^{-1}, $J_{dipolar}$ = 3.311 cm^{-1}, and $J_{dipolar}$ = 4.401 cm^{-1} for **1–3**, respectively. The values for **1** and **3** are rather similar due to the similar angle between the local magnetic axes of the two sites in the respective complexes. The value for **2** differs somewhat from those for the other two due to the different angle between the axes. A fit of the interaction parameters including both the intramolecular superexchange and the intermolecular dipolar coupling proved impossible because the two effects introduce a very similar but opposite effect to the magnetic susceptibility. Thus, a large number of different pairs of values could produce a very similar susceptibility and the parameters could not be extracted in an unambiguous manner. An attempt was made to fit the intramolecular exchange parameter by ignoring the intermolecular interactions. This, however, led to an anti-ferromagnetic interaction in all cases, which is at odds both with the BS-DFT calculations and with qualitative considerations based on the geometry of the bridges.

Based on both the BS-DFT calculations and the calculation of the dipolar interactions, the results show that the intramolecular interaction includes both a weak ferromagnetic superexchange component and ferromagnetic dipolar component. The intermolecular interaction is almost certainly anti-ferromagnetic as ignoring it in the fit leads to an incorrect anti-ferromagnetic intramolecular exchange parameter. In the case of **1** and **3** the sum of the intramolecular exchange and dipolar interaction is stronger than the intermolecular anti-ferromagnetic interaction, leading to a sharp increase in the $\chi_M T$ product at lower temperatures, which is indicative of ferromagnetic interaction. In the case of **2**, the $\chi_M T$ product shows no sudden increase at low temperatures, suggesting an overall anti-ferromagnetic interaction. This can be explained by the dominant intermolecular anti-ferromagnetic interaction. The intramolecular dipolar interaction is the weakest in **2** and the intermolecular contacts are the shortest.

In addition, the higher effective barrier found in complex **1** should arise from the coordination anion change. As an obvious contrast of **2** and **3**, it can be clearly observed that the only tfa^- anion pulls the two metal centers closer and even draws the vanillin-derived part of the two ligands closer through the Dy–N and Dy–O bonds (Fig. 9). To show this change more clearly, some pivotal parameters of the structure, such as the Dy–O (axial position) bond length (d_{Dy-O}), Dy–O–Dy angle, Dy⋯Dy distance, angle (θ) between the Dy–Dy line and the connection of each metal to its coordinating oxygen atom in the axial direction and the centroid of the triangle formed by three oxygen atoms on one side of the equatorial plane (d_{center}) have been listed in Table 1. It is obvious that **1** displays the shortest

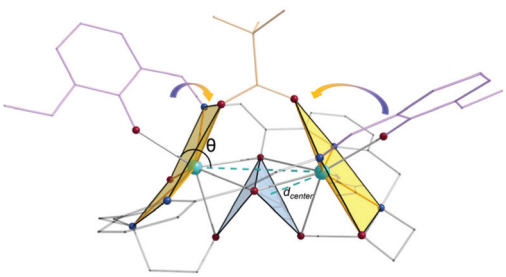

Fig. 9 Tractive effect of tfa^- (tan) on vanillin-derived part (lavender). The arrow shows the direction in which the vanillin-derived parts are pulled up.

Table 1 Some crucial structural parameters for complexes **1**, **2** and **3**

	1		**2**		**3**	
Complex	Dy1	Dy2	Dy1	Dy2	Dy1	Dy2
Dy⋯Dy/Å	4.026		4.111		4.134	
d_{Dy-O}/Å	2.194	2.184	2.224	2.247	2.199	2.212
d_{center}/Å	1.803	1.767	1.777	1.746	1.798	1.832
Dy–O–Dy/°	111.8	112.1	114.5	116.8	114.7	116.7
θ/°	146.8	145.3	155.1	148.8	148.0	153.7

d_{Dy-O} in the three complexes, leading to a stronger CF, and subsequently a higher effective barrier in **1**. Furthermore, a much shorter intramolecular Dy⋯Dy distance in **1** is also consistent with the larger calculated value of $J_{exchange}$.

Conclusions

The use of versatile hydrazone-based ligands and a careful tuning of the experimental conditions made possible the separation of three new Dy_2 SMMs (**1**, **2**, **3**), where two H_2L^{2-} ligands having two asymmetric pockets bridged by an enolate oxygen couple two Dy^{III} ions together. All Dy^{III} sites in complexes **1–3** show relatively axial crystal-fields dominated by the interaction with the Dy^{III} ion and the aryloxy oxygen of the ligands. The only exception is the Dy2 ion in complex **2**, where the presence of the methoxy ligand makes a contribution to the field, which is comparable to the aryloxy oxygen and leads to a destruction of the axiality. The intramolecular interaction is essential to suppress the local quantum tunneling of magnetization at the Dy^{III} sites and to allow slow relaxation of magnetization at zero field *via* the first local excited states. The interaction in these complexes consists of a ferromagnetic superexchange *via* the bridging oxygens, an intramolecular ferromagnetic dipolar interaction and an intermolecular anti-ferromagnetic dipolar field. The anti-ferromagnetic intermolecular interaction is critical to understanding the overall magnetic properties. The weakest intramolecular dipolar interaction and meanwhile the shortest intermolecular distance result in the dominant anti-ferromagnetic interaction, which leads to a continuous decrease of the $\chi_M T$ product.

Conflicts of interest

The authors declare no conflict of interest.

Acknowledgements

We thank the National Natural Science Foundation of China (Grants 21525103 and 21871247) and Key Research Program of Frontier Sciences, CAS (Grant ZDBS-LY-SLH023) for financial support. J. T. gratefully acknowledges support of the Royal Society-Newton Advanced Fellowship (NA160075). A. M. acknowledges funding provided by the Magnus Ehrnrooth Foundation and Kvantum Institute (University of Oulu). Computational resources were provided by CSC-IT Center for Science in Finland and the Finnish Grid and Cloud Infrastructure (persistent identifier urn:nbn:fi:research-infras-2016072533).

References

1 D. Gatteschi, R. Sessoli and J. Villain, *Molecular Nanomagnets*, Oxford University Press, Oxford, 2006.
2 C. Benelli and D. Gatteschi, *Introduction to Molecular Magnetism: From Transition Metals to Lanthanides*, Wiley-VCH Verlag GmbH & Co. KGaA, 2015.
3 J. L. Liu, Y. C. Chen and M. L. Tong, *Chem. Soc. Rev.*, 2018, **47**, 2431–2453.
4 F.-S. Guo, A. K. Bar and R. A. Layfield, *Chem. Rev.*, 2019, **119**, 8479–8505.
5 B. M. Day, F.-S. Guo and R. A. Layfield, *Acc. Chem. Res.*, 2018, **51**, 1880–1889.
6 A. Gaita-Arino, F. Luis, S. Hill and E. Coronado, *Nat. Chem.*, 2019, **11**, 301–309.
7 V. S. Denchev, S. Boixo, S. V. Isakov, N. Ding, R. Babbush, V. Smelyanskiy, J. Martinis and H. Neven, *Phys. Rev. X*, 2016, **6**, 031015.
8 C. Godfrin, A. Ferhat, R. Ballou, S. Klyatskaya, M. Ruben, W. Wernsdorfer and F. Balestro, *Phys. Rev. Lett.*, 2017, **119**, 187702.
9 N. Ishikawa, M. Sugita, T. Ishikawa, S. Koshihara and Y. Kaizu, *J. Am. Chem. Soc.*, 2003, **125**, 8694–8695.
10 D. N. Woodruff, R. E. P. Winpenny and R. A. Layfield, *Chem. Rev.*, 2013, **113**, 5110–5148.
11 *Lanthanides and Actinides in Molecular Magnetism*, ed. R. A. Layfield and M. Murugesu, Wiley-VCH Verlag GmbH & Co. KGaA, 2015.
12 F. S. Guo, B. M. Day, Y. C. Chen, M. L. Tong, A. Mansikkamaki and R. A. Layfield, *Science*, 2018, **362**, 1400–1403.
13 J. D. Rinehart, M. Fang, W. J. Evans and J. R. Long, *J. Am. Chem. Soc.*, 2011, **133**, 14236–14239.
14 Y. N. Guo, G. F. Xu, W. Wernsdorfer, L. Ungur, Y. Guo, J. Tang, H. J. Zhang, L. F. Chibotaru and A. K. Powell, *J. Am. Chem. Soc.*, 2011, **133**, 11948–11951.
15 J. Long, F. Habib, P. H. Lin, I. Korobkov, G. Enright, L. Ungur, W. Wernsdorfer, L. F. Chibotaru and M. Murugesu, *J. Am. Chem. Soc.*, 2011, **133**, 5319–5328.
16 T. Fukuda, K. Matsumura and N. Ishikawa, *J. Phys. Chem. A*, 2013, **117**, 10447–10454.
17 T. Pugh, N. F. Chilton and R. A. Layfield, *Angew. Chem., Int. Ed.*, 2016, **55**, 11082–11085.
18 Y. Horii, K. Katoh, B. K. Breedlove and M. Yamashita, *Chem. Commun.*, 2017, **53**, 8561–8564.
19 F. Habib, J. Long, P. H. Lin, I. Korobkov, L. Ungur, W. Wernsdorfer, L. F. Chibotaru and M. Murugesu, *Chem. Sci.*, 2012, **3**, 2158–2164.
20 Y. C. Chen, J. L. Liu, L. Ungur, J. Liu, Q. W. Li, L. F. Wang, Z. P. Ni, L. F. Chibotaru, X. M. Chen and M. L. Tong, *J. Am. Chem. Soc.*, 2016, **138**, 2829–2837.
21 J. Liu, Y. C. Chen, J. L. Liu, V. Vieru, L. Ungur, J. H. Jia, L. F. Chibotaru, Y. Lan, W. Wernsdorfer, S. Gao, X. M. Chen and M. L. Tong, *J. Am. Chem. Soc.*, 2016, **138**, 5441–5450.
22 A. B. Canaj, S. Dey, E. R. Martí, C. Wilson, G. Rajaraman and M. Murrie, *Angew. Chem., Int. Ed.*, 2019, **131**, 14284–14289.
23 S. Biswas, S. Das, T. Gupta, S. K. Singh, M. Pissas, G. Rajaraman and V. Chandrasekhar, *Chem. – Eur. J.*, 2016, **22**, 18532–18550.

24 G. Sheldrick, *Acta Crystallogr., Sect. A: Found. Adv.*, 2015, **71**, 3–8.
25 L. J. Bourhis, O. V. Dolomanov, R. J. Gildea, J. A. K. Howard and H. Puschmann, *Acta Crystallogr., Sect. A: Found. Adv.*, 2015, **A71**, 59–71.
26 O. V. Dolomanov, L. J. Bourhis, R. J. Gildea, J. A. K. Howard and H. Puschmann, *J. Appl. Crystallogr.*, 2009, **42**, 339–341.
27 E. A. Boudreaux and L. N. Mulay, *Theory and applications of molecular diamagnetism*, John Wiley & Sons, New York, 1976.
28 J. P. Perdew, K. Burke and M. Ernzerhof, *Phys. Rev. Lett.*, 1996, **77**, 3865–3868.
29 J. P. Perdew, K. Burke and M. Ernzerhof, *Phys. Rev. Lett.*, 1997, **78**, 1396–1396.
30 M. Ernzerhof and G. E. Scuseria, *J. Chem. Phys.*, 1999, **110**, 5029–5036.
31 C. Adamo and V. Barone, *J. Chem. Phys.*, 1999, **110**, 6158–6170.
32 M. Dolg, H. Stoll, A. Savin and H. Preuss, *Theor. Chim. Acta*, 1989, **75**, 173–194.
33 D. Andrae, U. Huermann, M. Dolg, H. Stoll and H. Preu, *Theor. Chim. Acta*, 1990, **77**, 123–141.
34 A. Schafer, C. Huber and R. Ahlrichs, *J. Chem. Phys.*, 1994, **100**, 5829–5835.
35 P. Siegbahn, A. Heiberg, B. Roos and B. Levy, *Phys. Scr.*, 1980, **21**, 323–327.
36 B. O. Roos, P. R. Taylor and P. E. M. Siegbahn, *Chem. Phys.*, 1980, **48**, 157–173.
37 P. E. M. Siegbahn, J. Almlöf, A. Heiberg and B. O. Roos, *J. Chem. Phys.*, 1981, **74**, 2384–2396.
38 P. Å. Malmqvist, B. O. Roos and B. Schimmelpfennig, *Chem. Phys. Lett.*, 2002, **357**, 230–240.
39 L. F. Chibotaru and L. Ungur, *J. Chem. Phys.*, 2012, **137**, 064112.
40 L. Ungur and L. F. Chibotaru, *Chem. – Eur. J.*, 2017, **23**, 3708–3718.
41 L. Ungur and L. F. Chibotaru, in *Lanthanides and Actinides in Molecular Magnetism*, Wiley-VCH Verlag GmbH & Co. KGaA, 2015, pp. 153–184.
42 M. E. Lines, *J. Chem. Phys.*, 1971, **55**, 2977–2984.
43 L. F. Chibotaru, L. Ungur and A. Soncini, *Angew. Chem., Int. Ed.*, 2008, **47**, 4126–4129.
44 L. Ungur, W. Van den Heuvel and L. F. Chibotaru, *New J. Chem.*, 2009, **33**, 1224–1230.
45 F. Aquilante, J. Autschbach, R. K. Carlson, L. F. Chibotaru, M. G. Delcey, L. De Vico, I. Fdez Galvan, N. Ferre, L. M. Frutos, L. Gagliardi, M. Garavelli, A. Giussani, C. E. Hoyer, G. Li Manni, H. Lischka, D. Ma, P. A. Malmqvist, T. Muller, A. Nenov, M. Olivucci, T. B. Pedersen, D. Peng, F. Plasser, B. Pritchard, M. Reiher, I. Rivalta, I. Schapiro, J. Segarra-Marti, M. Stenrup, D. G. Truhlar, L. Ungur, A. Valentini, S. Vancoillie, V. Veryazov, V. P. Vysotskiy, O. Weingart, F. Zapata and R. Lindh, *J. Comput. Chem.*, 2016, **37**, 506–541.
46 W. Kutzelnigg and W. Liu, *J. Chem. Phys.*, 2005, **123**, 241102.
47 M. Filatov, *J. Chem. Phys.*, 2006, **125**, 107101.
48 B. O. Roos, R. Lindh, P. A. Malmqvist, V. Veryazov and P. O. Widmark, *J. Phys. Chem. A*, 2004, **108**, 2851–2858.
49 B. O. Roos, R. Lindh, P. A. Malmqvist, V. Veryazov and P. O. Widmark, *J. Phys. Chem. A*, 2005, **109**, 6575–6579.
50 B. O. Roos, R. Lindh, P. A. Malmqvist, V. Veryazov, P. O. Widmark and A. C. Borin, *J. Phys. Chem. A*, 2008, **112**, 11431–11435.
51 L. Noodleman, *J. Chem. Phys.*, 1981, **74**, 5737–5743.
52 G. Jonkers, C. A. de Lange, L. Noodleman and E. J. Baerends, *Mol. Phys.*, 2006, **46**, 609–620.
53 L. Noodleman, J. G. Norman, J. H. Osborne, A. Aizman and D. A. Case, *J. Am. Chem. Soc.*, 1985, **107**, 3418–3426.
54 L. Noodleman and E. R. Davidson, *Chem. Phys.*, 1986, **109**, 131–143.
55 T. Yanai, D. P. Tew and N. C. Handy, *Chem. Phys. Lett.*, 2004, **393**, 51–57.
56 A. D. Becke, *Phys. Rev. A*, 1988, **38**, 3098–3100.
57 C. Lee, W. Yang and R. G. Parr, *Phys. Rev. B: Condens. Matter Mater. Phys.*, 1988, **37**, 785–789.
58 F. Weigend and R. Ahlrichs, *Phys. Chem. Chem. Phys.*, 2005, **7**, 3297–3305.
59 R. Gulde, P. Pollak and F. Weigend, *J. Chem. Theory Comput.*, 2012, **8**, 4062–4068.
60 R. Seeger and J. A. Pople, *J. Chem. Phys.*, 1977, **66**, 3045–3050.
61 R. Bauernschmitt and R. Ahlrichs, *J. Chem. Phys.*, 1996, **104**, 9047–9052.
62 V. Vieru, L. Ungur and L. F. Chibotaru, *J. Phys. Chem. Lett.*, 2013, **4**, 3565–3569.
63 D. Casanova, M. Llunell, P. Alemany and S. Alvarez, *Chem. – Eur. J.*, 2005, **11**, 1479–1494.
64 G. Cosquer, F. Pointillart, S. Golhen, O. Cador and L. Ouahab, *Chem. – Eur. J.*, 2013, **19**, 7895–7903.
65 L. Zhang, L. Zhao, P. Zhang, C. Wang, S. W. Yuan and J. Tang, *Inorg. Chem.*, 2015, **54**, 11535–11541.
66 D. I. Alexandropoulos, L. Cunha-Silva, L. Pham, V. Bekiari, G. Christou and T. C. Stamatatos, *Inorg. Chem.*, 2014, **53**, 3220–3229.
67 S. Biswas, L. Mandal, Y. Shen and M. Yamashita, *Dalton Trans.*, 2019, **48**, 14096–14102.
68 Y. N. Guo, G. F. Xu, Y. Guo and J. Tang, *Dalton Trans.*, 2011, **40**, 9953–9963.
69 D. Reta and N. F. Chilton, *Phys. Chem. Chem. Phys.*, 2019, **21**, 23567–23575.
70 P. Moreira Ide and F. Illas, *Phys. Chem. Chem. Phys.*, 2006, **8**, 1645–1659.